Active Implantable Sensor Powered by Ultrasounds With Application in the Monitoring of Physiological Parameters for Soft Tissues

Bruno M. G. Rosa
Imperial College London
South Kensington Campus
London SW7 2AZ, UK
Email: b.gil-rosa@imperial.ac.uk

Guang Z. Yang
Imperial College London
South Kensington Campus
London SW7 2AZ, UK
Email: g.z.yang@imperial.ac.uk

***Abstract*—Ultrasound imaging is a proven diagnostic tool to assess a myriad of physiological and pathological conditions in patients. Throughout the years, ultrasounds have been used as a passive recording modality where the backscattered echo arising from the interaction of the sound waves with the acoustic properties of the biological tissues helps to identify them. Apart from a wide range of therapeutic applications, the acoustic beam has not yet been explored to actuate within the biological environment in an active way. In this paper we present an implantable electronic device to be actuated remotely by ultrasounds with capabilities for measuring several physiological parameters of tissues: pH, temperature, electrolyte concentration and biopotentials. The small factory form device (with no attached batteries) harvests energy from the incoming ultrasound waves and uses it to power the embedded electronics. It operates from voltage levels as low as 0.8 V and consuming a total current of 60 μA (or an average power consumption of 84 μW) in the active mode when deployed at a distance of 3 cm from the active source of ultrasounds *in vitro*, excited by a sinusoid at 400 kHz with power density of 20 mWcm^{-2}. The sensor can be actuated by a specifically-designed readout device (as detailed in this paper) or using the traditional medical probes for ultrasound imaging. The actual device can present an alternative to surpass the limitations of inductive and RF-powered sensors implanted in soft tissues.**

I. Introduction

Ultrasounds (US) have been used for the past decades in medical imaging to evaluate several physiological processes, with a particular emphasis on breast cancer scanning, foetal development assessment in pregnant women and blood flow measurements [1]. The widespread of ultrasound imaging as a non-invasive modality for diagnostic and therapeutic applications has led to the development of a range of ultrasound machines with different characteristics and sizes that are indispensable in the equipment of every major hospital or clinic. The physics of transdution in US is based on the piezoelectricity principle found in some materials that converts mechanical strains into an electric voltage and vice-versa. The type, size and arrangement of the ultrasonic transducer (or array) dictates the operational frequency (typically between 0.4 - 10 MHz), penetration depth and apodization of the acoustic beam for the different imaging modalities offered by US [2]. Although massively used by clinicians in their practice, the acoustic beams are still to be explored for purposes other than imaging or therapy in the medical context, videlicet to operate remotely implanted sensors within the human body.

The topics of power harvesting and data exchange for implantable sensors are becoming increasingly popular in the research community, where competitive (and complementary) technologies have been proposed in recent years to retrieve the largest amount of physiological information from patients while expending the lowest power consumption possible in the sensor electronics [3]. Energy sources available for sensors deployed inside a physiological environment include electrochemical [4], photovoltaic [5], thermoelectric [6], mechanical [7], magnetic (inductive) [8], electromagnetic (RF) [9] and ultrasounds [10]. The efficiency in conversion to readily in-use electrical energy dictates that, for the time being, only inductive near-field, far-field RF and ultrasounds have the potential to fulfil the power requirements of the embedded electronics in the sensor. The major advantages of employing ultrasonic links is that the power transfer efficiency can, theoretically, be made higher and the link is immune to EM interferences caused by the operation of nearby electronic devices either inside (e.g. pacemakers) or outside the body (larger ferromagnetic objects).

The area of implantable electronics has already produced some commercially successful devices like cardiac pacemakers and defibrillators, neurologic stimulators, drug pump systems and cochlear implants [11]. The constrains in the physical dimension and location of these devices, together with the power consumption requirements, all settle the framework for achieving the *acceptable* level of operation of the implant without causing side effects [12]. The complexity of the electronics to correctly sense, process and transmit the data has a direct impact on power consumption which, in turn, increases the physical volume for energy conversion and storage [9]. Batteries impose a life-term to the implant (10 years at best) and a surgical intervention for replacement.

Rechargeable batteries and similar components [13] are currently being developed to alleviate some geometrical constrains by means of flexible and stretchable materials that can really reshape the future of implantable sensor packaging [14]. However, the need for wireless transmission of energy to recharge the storage components at the implant side still remains [15]. Even in the condition of zero-powering experienced by some *passive* sensors, there must be some energy convoy to interrogate and capture the physical property reflected back by the implant [16]. Both operations will keep functional as long as the link is active, which might be sufficient to record the physiological variables of interest.

It is the objective of this paper to describe the electronics involved in the design of an active implantable sensor and external readout device using ultrasounds, while providing some insights into the imaging technique that mediates the interaction between body tissues and sound waves. Clinical applications include the evaluation of the physiological state of a tissue, complementary to the anatomical image produced by ultrasound imaging, as in the case of assessing local infections and complications after surgery in soft tissues.

II. Material and Methods

This section details the computational framework developed to describe the interaction between sound waves and tissues, where important parameters such as pressure fields experienced by the implant and acoustic impedance of the transmission line, can be tested to provide minuteness in the design of both the implantable sensor and scanning probe.

A. Forward Problem in Ultrasounds

The power delivered to the implantable device depends on the distribution of the acoustic pressure field generated by the transmitting piezoelectric transducer and the layers of biological tissues in the path. The knowledge of the physics underlying sound wave propagation can help establishing the preferential location and orientation of the implantable sensor in the radiated area within safe exposure limits for biological tissues ($\leq$ 94 mWcm^{-2}). However, the mathematical relations involved can hardly be solved in a closed form and so, numerical approximations are implemented to obtain an estimation of the fields at stake. Within this approach, the total field is given by a summation of the incident pressure field (in the absence of scatterers in the medium) and the scattered pressure field, in accordance to Expression 1.

$$p^{tot}(\mathbf{x}) = p^{inc}(\mathbf{x}) + p^{sct}(\mathbf{x}) \tag{1}$$

Further developments over the term $p^{sct}(\mathbf{x})$ proceeding from wave scattering theory [17], helps to re-written the integral full wave equation as,

$$p^{tot}(\mathbf{x}) = p^{inc}(\mathbf{x}) + \int_{\mathbf{x'}\in\mathbb{D}} \mathcal{G}(\mathbf{x}-\mathbf{x'})\Delta\gamma p^{tot}(\mathbf{x'})dV + \\ + \int_{\mathbf{x'}\in\mathbb{D}} \mathcal{G}(\mathbf{x}-\mathbf{x'})\{\nabla\cdot[\Delta\rho\nabla p^{tot}(\mathbf{x'})]\}dV \tag{2}$$

where $\Delta\gamma$ and $\Delta\rho$ are contrast functions that account for the differences in the complex propagation coefficient γ (attenuation) and volume-mass density ρ, respectively; ∇ is the topological gradient operator whereas $\nabla\cdot$ is the divergence; and $\mathcal{G}$ is the Green's function. The full wave equation just described can be represented in the form of a linear system by imposing a forward operator, $\mathcal{L}$, that maps all the topological relations and properties at any point $\mathbf{x}$ in the domain to the remaining points, as Expression 3 attests.

$$p^{inc}(\mathbf{x}) = \mathcal{L}[p^{tot}(\mathbf{x})] \tag{3}$$

The solution for the equation in terms of the total pressure field can be solved numerically by resorting to iterative methods whenever the incident field is known in advance. The Conjugate Gradient (CG) method approximates the solution of the field with an iterative step of the form,

$$\begin{cases} \mathbf{p_0} = \mathbf{0} \\ \mathbf{p_{n+1}} = \mathbf{p_n} + \alpha_\mathbf{n}\xi_\mathbf{n} \end{cases} \tag{4}$$

where $\mathbf{p}_0$ is the initial estimate for the total pressure field (null vector), $\mathbf{p}_{n+1}$ is the updated pressure, α_n the step size and ξ_n the update direction. The residual field accounting for the differences from the incident field and normalized error to control the convergence of CG are both given by Expression 5.

$$\begin{cases} \mathbf{r_n} = \mathbf{p^{inc}} - \mathcal{L}[\mathbf{p_n}] \\ error = \frac{||\mathbf{r_n}||_\mathbb{D}}{||\mathbf{p^{inc}}||_\mathbb{D}} \end{cases} \tag{5}$$

Finally, the incident field is pre-computed and stored in memory before the CG routine takes place, by spatially convolving the geometrical model of the transducer (source) with the Green's function for a background medium as [18],

$$p^{inc}(x) = \imath\omega\rho_0 \int_{\mathbf{x'}\in\mathbb{D}} \mathcal{G}(\mathbf{x}-\mathbf{x'})s(\mathbf{x'})dV \tag{6}$$

where $s(\mathbf{x'})$ is the source term, ω the angular frequency and ρ_0 the volume-mass density of the background.

Simulations for 2D using a realistic biological phantom are shown in *fig. 1*. The domain represents a transversal slice of the human torso at the level of the third intercostal space (no blocking bones), with image dimensions of 128 x 64 *pixels*. All biological tissues are assigned acoustic properties as found in literature [1], namely density, speed of sound propagation and attenuation coefficient. The implantable sensor is located in the pericardium of the heart with changing acoustic properties that will reshape the data transmission mechanism between the implant and transmitting transducer in subsequent sections.

B. Electronic Design

1) Implantable Sensor: The first electronic stage directly connected to the commercial piezoelectric transducer consists of a voltage doubler interface as illustrated in *fig. 2 b)*. The transducer can be modelled as a sinusoidal current source in parallel with an high internal capacitance, C_0, that limits power extraction from the harvester. So it is not only important to excite the transducer close to its resonant frequency (400 kHz), but also to employ an inductor in series to maximize power transfer to the rest of the electronic circuit (load). When the voltage signal produced is positive for half

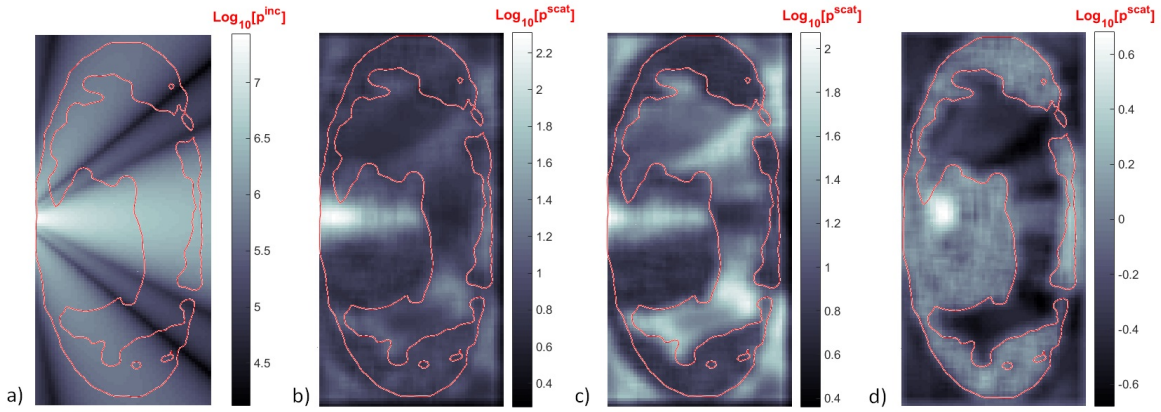


Fig. 1. Numerical simulations of the pressure fields in a 2D transversal slice of the human torso, with anatomical contour lines superimposed in red: a) incident field; b) scattered field obtained when the implant has the same properties as heart muscle; c) scattered field when the implant has different properties with respect to biological tissues; d) difference in the aforementioned scattered fields that pinpoints the location of the implant (lighter area).

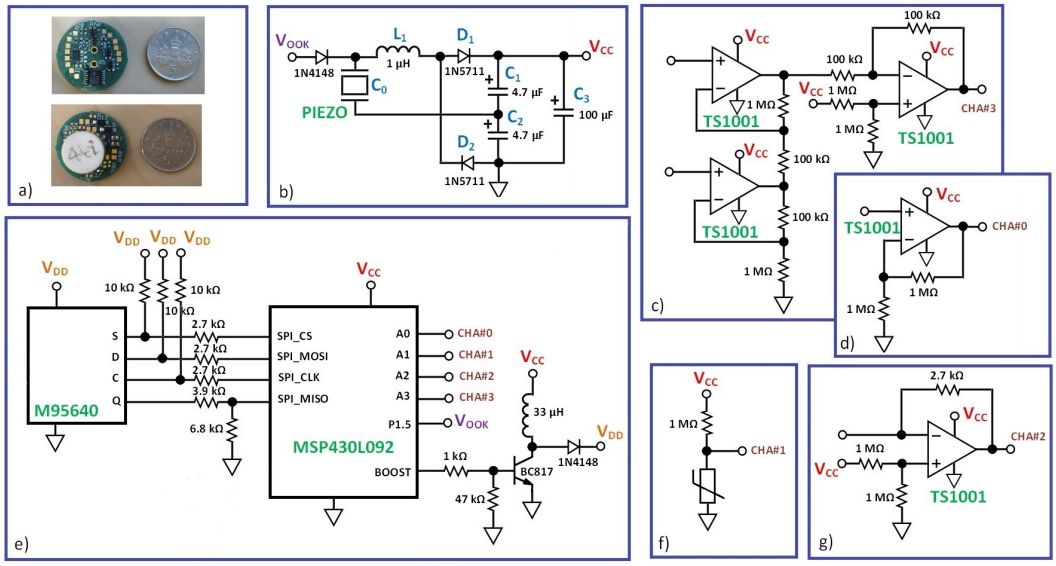


Fig. 2. Simplified diagram of the electronics composing the implantable sensor: a) top and bottom views; b) voltage doubler interface; c) instrumentation amplifier; d) non-inverting amplifier; e) micro-controller unit with booster circuit; f) temperature-controlled voltage divider; g) inverting amplifier.

the cycle, diode D_1 is conducting while D_2 is off, charging capacitor C_1; by its turn, in the negative half cycle, the status of both diodes exchange and C_2 is charged. This way, the interface provides an extra improvement in efficiency since the voltage delivered to the load, V_{CC}, is twice the one provided by the four diode-bridge rectifier. Although the maximum power output is equal for both interfaces, the simple fact of using just two diodes in the doubler limits the voltage drop caused by the diode forward voltages (which is 400 mV for the 1N5711).

DC voltage levels stored in the larger capacitor C_3 can peak as high as 10 V in the condition of no load and with the transducer facing directly the source of the ultrasonic beam. When loading the circuit, the voltage will drop dramatically in order to provide for the electric current consumed by circuit electronics. If one intends to keep a voltage operation for the sensor around 1 V, a total circuit load of 10 kΩ is fairly required to keep the discharging time of C_3 in the order of seconds and still accommodating a current of 100 μA. So, only ultra-low-power components were considered for the design of the implantable sensor. The choice for the micro-controller (MCU) fell over the MSP430L092 from Texas Instruments which exhibits a current consumption of 45 μA with 1 MHz instruction frequency and a voltage range of operation from 0.8 V to 1.5 V. The only drawback is the romless nature of the MCU that implies an external EEPROM to store the 2 kB program code. The MCU is already equipped with the boot sequence to read data from an high-speed memory with serial SPI bus capability as long as signal logics remain at the correct voltage levels. Since there is still no EEPROM that can operate as low as 1 V, a voltage booster is required to increase the level of V_{CC} to the higher value of V_{DD}. The booster topology adapted is shown in *fig. 2 e)* which uses the duty-cycle of the PWM signal

produced by the digital pin labelled BOOST and transistor BC817 to raise V_{DD} to 1.8 V, necessary to transfer the data from the EEPROM - the M95640 from ST Semiconductors - to the MCU within a few milliseconds.

The analogue part of the implantable sensor includes four different modules designed with standard opamp configurations: an inverting amplifier for electrolyte measurements (lactate/glucose), a non-inverting amplifier for pH measurements, an instrumentation amplifier for biopotential recordings and a voltage divider for temperature measurements (thermistor). The attractive characteristics of the modules are the employment of an ultra-low-power opamp - the TS1001 from Silicon Labs - which consumes only 0.6 μA *per* amplifier (while operating between 0.5 - 2.5 V) and the large values set to the resistors in order to limit current consumption by the circuit. A level of 60 μA is achieved when all the electronic components (except EEPROM) are in the active mode of operation.

The voltage levels recorded by each analogue module are digitalized by the internal ADC of the MCU (8-bit of resolution) and sampled sequentially within a time period of 10 ms. The data transmission packet includes also two signalling bytes that convoy a bit-pattern to be recognized by the external readout device. One digital pin of the MCU is used to shift-out the bit-pattern using ON-OFF keying modulation (OOK) directly over the input terminal of the transducer. Since the ultrasonic beam uses a frequency of 400 kHz to transmit the energy from outside the body, exciting the same line with a lower frequency for data transmission does not compromise the operation of the harvester as long as the line is de-coupled by a 1N4148 diode, as depicted in the graphic of *fig. 3*.

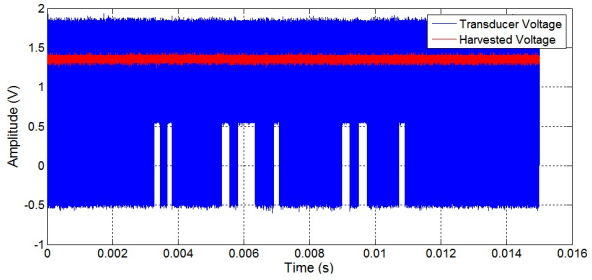


Fig. 3. Temporal recording of the DC level harvested by the sensor (red line) and voltage signal at the piezoelectric transducer (blue line) with OOK modulation superimposed over the 400 kHz sine wave. The bit pattern shown corresponds to 4 bytes: 10100000 10110010 00000000 10100001.

2) Scanning Probe: The external device must be able to provide energy in the form of ultrasounds to the implantable sensor at the same time it correctly tracks the data sent by the latter. The circuit for the scanning probe can be divided into two modules - ultrasound wave generation and detection - as illustrated in *fig. 4*. The micro-controller employed is the PIC32MZ1024 from Microchip with a cycle frequency of 200 MHz that enables the control of all operations in the scanning probe, including the routing of the data from the implantable sensor to a host computer *via* USB or Bluetooth.

The generation of the ultrasound wave is the responsibility of a precision timing circuit - the NE555 from Texas Instruments - working in *astable* mode. The circuit is tuned to produce a TTL signal with frequency of 400 kHz and 5 V of amplitude. Further conditioning of the signal by means of wideband opamps allow to remove the DC component of the TTL signal, followed by low-pass filtering to eliminate higher order harmonics (achieving a sinusoid), before splitting the wave into two out-of-phase branches that will excite simultaneously the transducer. The 180° phase difference is achieved by feeding the sine wave to an inverter amplifier - the OP275 from Analog Devices - with unitary gain and, then, taking both the input and output signals to produce the two out-of-phase branches. The piezoelectric element is, this way, excited by twice the voltage level which yields an higher pressure field with an intensity close to 20 mWcm^{-2}.

Tracking of the digital data sent by the implantable sensor is based on the *backscaterring* process, that is, modulation of the backscattered ultrasound energy by changing the electrical impedance of the implantable transducer as seen by the external circuit. The KLM model of a piezoelectric transducer defines the resonator as a three-port network with two acoustic ports and one electrical port [1]. A modification of the circuit load induced by OOK modulation will change the acoustic impedance of the implantable transducer which, in turn, changes the reflectivity of the transmission line connecting to the readout transducer, quite in a similar way like the previous numerical simulations have shown. This change is manifested as a temporal tiny variation on the amplitude of the out-of-phase voltage signals at the readout transducer. So, in order to record the variations, the signals coming from the transducer are first buffered and amplified before feeding them to a demodulator, built around the AD633 from Analog Devices. The demodulator implements the mathematical function of squared differences as Expression 7 certifies.

$$V_{DEM} = \frac{(V_{S1} - V_{S2})(V_{S1} - V_{S2})}{10} \tag{7}$$

In the temporal domain, the operation corresponds to the multiplication of two sinusoids with the same frequency, relative similar amplitudes and 180° de-phased, yielding an output signal of the form,

$$v_{DEM}(t) = \frac{A_{12}}{20} * [\cos(180^\circ) + \cos(2 * (2\pi * 400 \times 10^3) + 180^\circ)] \tag{8}$$

where the coefficient A_{12} is the difference in amplitude between the two sinusoids. Low-pass filtering of $v_{DEM}(t)$ removes the component corresponding to twice the frequency of excitation, leaving only the DC term of the signal that carries the relevant information. The DC value is further amplified before been digitalised by the MCU with a sampling rate of 10 kSPS and 12-bit of resolution. Whenever the two signalling bytes within the data transmission packet are correctly identified by the MCU, the information proceeding from the implantable sensor is decoded and sent to the computer.

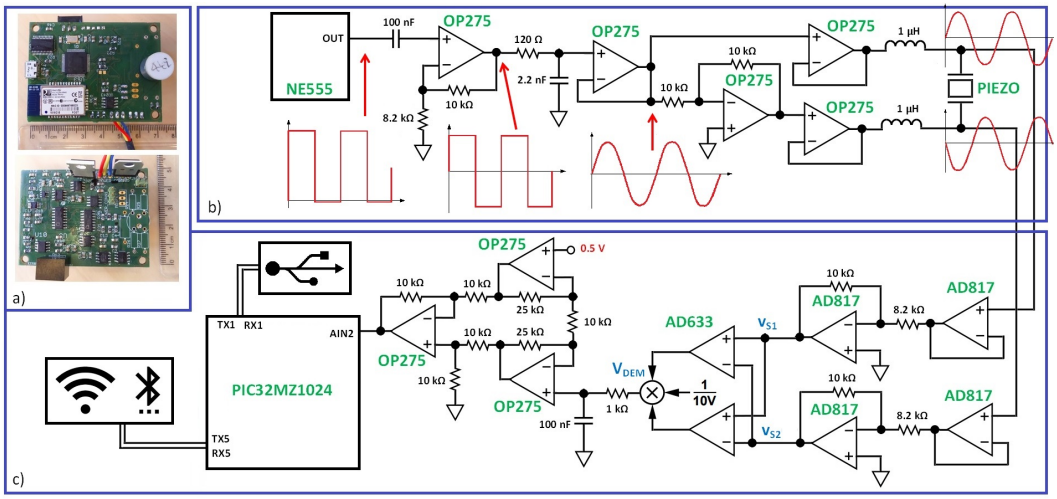


Fig. 4. Schematics of the scanning probe (readout device) developed for active ultrasound sensing, highlighting the main electronic components involved: a) top and bottom views; b) Ultrasound wave generation module; c) *Backscaterring* detection and data transmission module.

III. Results

The implantable sensor was tested in an experimental set-up consisting, firstly, of a PDMS transmission line connecting the piezo transducers, followed by the incorporation of a lung model to mimic a realistic torso phantom, *vide fig. 5*. PDMS is a biocompatible material with acoustic properties similar to biological tissues (namely fat), which can make it a good candidate for future sensor packaging. PDMS material was first cooked as a 10 x 10 cm^2 sheet with 2 mm of thickness and then cut into smaller pieces to be stacked together.

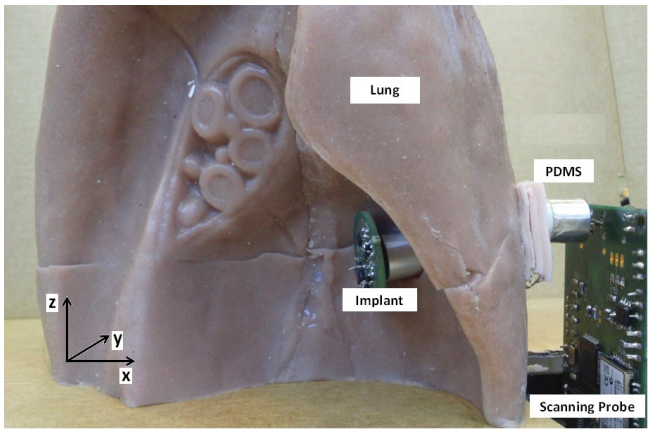


Fig. 5. Set-up apparatus developed to test the implantable sensor using a realistic phantom made of a lung (silicon) and fat tissue (PDMS).

Figures 6 and 7 show the DC level obtained by the harvester when the implantable sensor moves along the axis of the acoustic beam and off-axis, respectively, and with no lung tissue in-between. By its turn, *fig. 8* exhibits a data recording retrieved from the complete phantom for temperature, biopotential, pH and lactate measurements, the last ones obtained with electrodes attached to calibrated laboratory solutions to resemble a physiological environment.

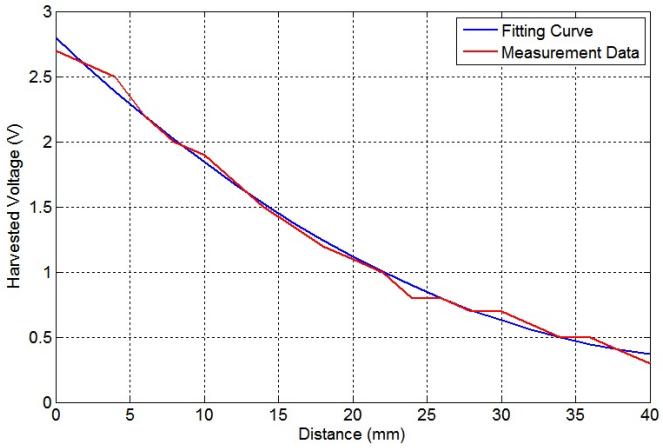


Fig. 6. Voltage level harvested by the implantable sensor as a function of the distance to the scanning probe transducer, with gap in-between filled by PDMS material (x-direction).

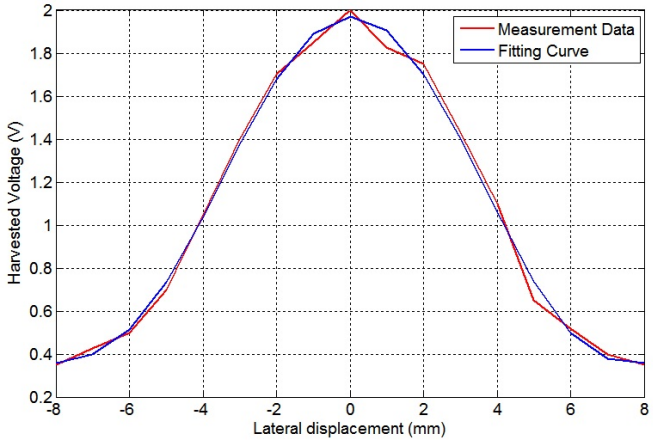


Fig. 7. Voltage level harvested by the implantable sensor as a function of the lateral displacement (in the y-direction) of the implantable transducer relative to the axis of the transmitting one (PDMS gap equal to 1 cm).

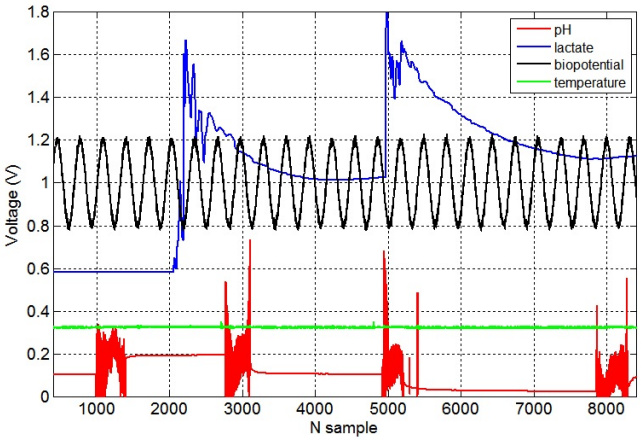


Fig. 8. Extended recording obtained for the acquisition channels within the implantable sensor with the complete phantom (gap = 2 cm). pH is recorded from calibrated solutions with different values: 6, 4, again 6 and 10. Lactate is obtained from solutions with concentrations 0.5, 4, and 8 mmol/L. Biopotential channel is fed from a waveform function generator, producing a 20 mV slowly varying sinusoid, while temperature remains constant during experiments (20° C).

IV. Conclusion

An implantable sensor to be deployed within a physiological environment has been described with ultrasonic powering and data transmission capabilities. The device proved to be fully functional up to 2.5 cm from the scanning probe, tracking correctly the variations on the physiological parameters *in vitro*. The harvested voltage profile obtained has shown an exponential decay with the distance from the transmitting transducer and a Gaussian-like shape for off-axis misalignments between the implantable and transmitting transducers. The results also demonstrate that the analogue modules of the sensor can operate up to greater distances (3.5 cm) when the harvested voltage drops below 0.5 V, though the MCU is already turned off for these levels. For the scenario where the sensor is expected to be deployed even deeper in the body while keeping the data telemetry functionality, the entire digital part of the sensor can be replaced by an analogue resonator circuit designed around the same ultra-low-power opamp employed in this project, and whose resonant frequency will change according to the voltage level being recorded, much like in a typical FSK modulation scheme. Using techniques other than amplitude modulation to code information helps to compensate for acoustic signal attenuation produced by biological tissues, at the expense of requiring a larger bandwidth for data transmission and a two-level voltage detector (ON-OFF) in the readout device instead of a full analogue range. However, the absence of a digital controller might lead to data security issues since encryption schemes or signalling codes are much hard to implement in the analogue domain.

Another important improvements to the implantable sensor include the replacement of the bulky transducers by smaller ones that are more suitable to conduct *in vivo* experiments. The change in dimensions will imply a shift in the operational frequency that can be easily accommodated by the electronics developed so far for both the implantable sensor and scanning probe. The re-design of the circuit board using flexible substrates is also an option for the implant to conform to the natural contours of tissues, as in the case of the anastomosis ring used to reconnect segments in the intestine after surgery.

Regarding power harvesting, advances in MEMS technology have already produced some ultrasound generators. However, the nanowatts range achieved is still two orders of magnitude below the power requirements for electronic components others than custom-made *lab-on-chip* sensors.

Acknowledgment

The authors would like to thank to the Engineering and Physical Science Research Council for the financial support under the project grant "EPSRC EP/L014149/1".

References

[1] Szabo, T. L., *Diagnostic Ultrasound Imaging: Inside Out.* Elsevier, Inc., London, 2004.

[2] Basak, A. *et al.*, *Implantable Ultrasonic Imaging Assembly for Automated Monitoring of Internal Organs.* IEEE Transactions on Biomedical Circuits and Systems, vol. 8, no. 6, 2014.

[3] Bazaka, K. and Jacob, M. V., *Implantable Devices: Issues and Challenges.* Electronics, vol. 2, pp. 1 - 34, 2013.

[4] Olivo, J. *et al.*, *Biofuel Cells and Inductive Powering as Energy Harvesting Techniques for Implantable Sensors.* Science of Advanced Materials, vol. 3, pp. 420 - 425, 2011.

[5] Sankaragomathi, K. *et al.*, *A 27 μW subcutaneous wireless biosensing platform with optical power and data transfer.* IEEE Proceedings of the Custom Integrated Circuits Conference, pp. 1 - 4, 2014.

[6] Rozgic, D. and Markovic, D., *A 0.78 mW/cm^2 Autonomous Thermoelectric Energy-Harvester for Biomedical Sensors.* Symposium on VLSI Circuits Digest of Technical Papers, 2015.

[7] Zhang, H. *et al.*, *A flexible and implantable piezoelectric generator harvesting energy from the pulsation of the ascending aorta: in vitro and in vivo studies.* Nano Energy, vol. 12, pp. 296 - 304, 2015.

[8] Kiani, M. and Ghovanloo, *A 13.56 Mbps pulse delay modulation based transceiver for simultaneous near-field data and power transmission.* IEEE Transactions on Biomedical Circuits and Systems, vol. 9, no. 1, 2015.

[9] Ba, A. *et al.*, *A 0.33 nJ/bit IEEE802.15.6/Proprietary MICS/ISM Wireless Transceiver With Scalable Data Rate for Medical Implantable Applications.* IEEE Journal of Biomedical And Health Informatics, vol. 19, no. 3, 2015.

[10] Fowler, A. *et al.*, *An Omnidirectional MEMS Ultrasonic Energy Harvester for Implanted Devices.* Journal of Microelectromechanical Systems, vol. 23, no. 6, 2014.

[11] Camara, C. *et al.*, *Security and privacy issues in implantable medical devices: A comprehensive survey.* Journal of Biomedical Informatics, vol. 55, pp. 272 - 289, 2015.

[12] Baker, M. W. and Sarpeshkar, R., *Feedback analysis and design of RF power links for low-power bionic systems.* IEEE Transactions on Biomedical Circuits and Systems, vol. 1, no. 1, 2007.

[13] Pech, D. *et al.*, *Ultrahigh-power micrometre-sized supercapacitors based on onio-like carbon.* Nature Nanotechnology, vol. 5, 2010.

[14] Xu, S. *et al.*, *Strechable batteries with self-similar serpentine interconnects and integrated wireless recharging systems.* Nature Communication, 2013.

[15] Ozeri, S. and Shmilovitz, D., *Ultrasonic transcutaneous energy transfer for powering implanted devices.* Ultrasonics, vol. 50, pp. 556 - 566, 2010.

[16] Chen, L. *et al.*, *Continuous wireless pressure monitoring and mapping with ultra-small passive sensors for health monitoring and critical care.* Nature Communications 5:5028, 2013.

[17] Dongen, K. *et al.*, *A forward model and conjugate gradient inversion technique for low-frequency ultrasonic imaging.* Journal of Acoustical society of America, vol. 120, no. 4, 2006.

[18] Wang, L. V. and Yang, X., *Boundary conditions in photoacoustic tomography and image reconstruction.* Journal of Biomedical Optics, vol. 12, no. 1, 2007.